Draft version October 26, 2026
Typeset using LaTeX **twocolumn** style in AASTeX7.0.1

arXiv:2610.32430v1 [astro-ph.GA] 23 Oct 2026

Local Analogs of Little Red Dots: Clues to the X-ray Weakness

Shi-Jiang Chen [1,2] Jun-Xian Wang [1,2,3] Zhen-Ya Zheng [4] Ruqiu Lin [4,5] Luis C. Ho [6,7] Zhen-Yi Cai [1,2] Chang-Hao Chen [6,7] Zsofi Igo [8] Jia-Lai Kang [1,2] Ruancun Li [9] Teng Liu [1,2] Wenke Ren [4] and Zhen-Bo Su [1,2]

[1] *Department of Astronomy, University of Science and Technology of China, Hefei 230026, People's Republic of China*
[2] *School of Astronomy and Space Science, University of Science and Technology of China, Hefei 230026, People's Republic of China*
[3] *College of Physics, Guizhou University, Guiyang, Guizhou, 550025, People's Republic of China*
[4] *Shanghai Astronomical Observatory, Chinese Academy of Sciences, 80 Nandan Road, Shanghai 200030, People's Republic of China*
[5] *University of Massachusetts Amherst, 710 North Pleasant Street, Amherst, MA 01003-9305, USA*
[6] *Kavli Institute for Astronomy and Astrophysics, Peking University, Beijing 100871, China*
[7] *Department of Astronomy, School of Physics, Peking University, Beijing 100871, China*
[8] *European Space Agency (ESA), European Space Astronomy Centre (ESAC), Camino Bajo del Castillo s/n, E-28692 Villanueva de la Cañada, Madrid, Spain*
[9] *Max-Planck-Institut für Extraterrestrische Physik (MPE), Giessenbachstrasse 1, 85748 Garching bei München, Germany*

ABSTRACT

A major question about JWST's little red dots (LRDs) at $z \sim 4-8$ is the origin of their apparent X-ray weakness. Even deep Chandra stacks yield only tentative detections or broad-band limits and cannot distinguish among super-Eddington accretion, intrinsic X-ray weakness, and Compton-thick (CT) obscuration. Local analogs offer a powerful complementary route. At $z \sim 0.3$, similarly luminous sources require $\sim 10^{3-4}$ less exposure for comparable signal-to-noise, suffer less source confusion, and directly probe the diagnostic rest-frame soft X-rays. Here we present a pilot Einstein Probe/FXT study of six "local little red dots" (LLRDs), V-shaped broad-line green pea galaxies selected as low-redshift counterparts of LRDs. These sources show X-ray diversity: "X-normal" LLRDs resemble type 1 AGNs in X-ray luminosity and optical variability, whereas "X-weak" stack lies ∼0.5–0.7 dex below standard unobscured-quasar scaling relations while remaining compatible with the representative LRD stack and 95 % of published individual limits. The X-weak LLRDs also lack detected optical variability and have redder optical continua than X-normal LLRDs, making their V-shaped SEDs closer to those of high-redshift LRDs. The detection of the X-weak stack at $\sim 3.3\sigma$ with the soft-X-ray-sensitive EP-FXT provides rest-frame $\sim 2-3$ keV constraints difficult to reconcile with a typical unobscured super-Eddington model or a local-AGN-like CT geometry examined here, although modified variants remain possible. The simplest alternative is a mildly X-ray-weak corona ($\Delta\alpha_{\rm ox} \sim -0.1$ to -0.2) with Compton-thin absorption ($N_{\rm H} \sim 10^{22-23}\,{\rm cm}^{-2}$), consistent with the independent Balmer decrement/break diagnostics. Together with growing samples of local LRD analogs, our results offer a practical path for testing the physical nature of LRD X-ray weakness.

Keywords: Active galactic nuclei (16) — Dwarf galaxies (416) — High-redshift galaxies (734) — X-ray astronomy (1810)

Corresponding author:
Shi-Jiang Chen, Jun-Xian Wang,
Zhen-Ya Zheng, Ruqiu Lin
csj666@mail.ustc.edu.cn, jxw@ustc.edu.cn,
zhengzy@shao.ac.cn, ruqiulin@umass.edu

1. THE LRD X-RAY BOTTLENECK

JWST has revealed an abundant population of enigmatic galaxies at $z \sim 4-8$ that are extremely compact and exhibit characteristic "V-shaped" rest-frame UV-to-optical spectral energy distributions (SEDs), now commonly referred to as "little red dots" (LRDs; Y. Harikane et al. 2023; J. Matthee et al. 2024; J. E. Greene et al. 2024; D. D. Kocevski et al. 2025; I. Labbe et al. 2025; C. Zhang et al. 2026). Broad permitted emission

lines with widths of $\gtrsim 10^3\,\mathrm{km\,s^{-1}}$ are found in a substantial fraction of LRDs, strongly suggesting accretion onto massive BHs. Nevertheless, the conventional multi-wavelength signatures of AGNs are often weak or absent (e.g., H. B. Akins et al. 2025; B. Wang et al. 2026). In particular, LRDs are rarely detected individually in X-rays (e.g., T. T. Ananna et al. 2024), apart from a small number of exceptions (e.g., S. Fu et al. 2026; R. E. Hviding et al. 2026). Stacking analyses totaling tens to hundreds of megaseconds have yielded only tentative signals or nondetections. When compared with the X-ray luminosities expected from standard AGN relations, these measurements indicate that LRDs are X-ray faint on average (M. Yue et al. 2024; A. Sacchi & Á. Bogdán 2025). Similar X-ray weakness has also been reported among the broader population of JWST-selected high-redshift AGNs (e.g., R. Maiolino et al. 2025; M. Brazzini et al. 2026; A. Comastri et al. 2026), possibly suggesting a common physical condition in rapidly growing BHs in the early universe.

Several scenarios have been proposed to explain this apparent population-level X-ray deficit. LRDs may host intrinsically weak or unusually soft X-ray coronae. In particular, super-Eddington accretion can produce steep X-ray spectra (photon index $\Gamma \sim 3$–4; F. Pacucci & R. Narayan 2024; K. Inayoshi et al. 2025; S. Zhou et al. 2026; E. Lambrides et al. 2026), leaving few detectable photons in the rest-frame hard X-rays sampled by Chandra at $z \sim 4$–8. Rapid accretion would also help explain how BHs reach inferred masses of $\sim 10^{7-8}\,M_\odot$ so early in cosmic history without requiring extremely massive seeds (e.g., V. De Luca et al. 2020; G.-W. Yuan et al. 2024). Alternatively, absorption by dense nuclear gas may suppress the observed X-ray emission. Strong evidence for such gas comes from the combined presence of Balmer absorption, prominent Balmer breaks, red optical continua, and elevated broad-line Balmer decrement—the "ABCD" diagnostics (C.-H. Chen et al. 2026; K. Inayoshi & L. C. Ho 2025; see also I. Juodžbalis et al. 2024; X. Ji et al. 2025; R. P. Naidu et al. 2025; S.-J. Chang et al. 2026; M.-Y. Zhuang et al. 2026; J. Matthee et al. 2026; I. Juodžbalis et al. 2026). Together, these features can be explained self-consistently by a dense, optically thick nuclear medium with $n_\mathrm{H} \gtrsim 10^9\,\mathrm{cm^{-3}}$, $N_\mathrm{H} \gtrsim 10^{22}\,\mathrm{cm^{-2}}$ and substantial covering factor in at least some systems. Such an environment makes X-ray obscuration a natural possibility, and extreme CT columns of $N_\mathrm{H} \gtrsim 10^{24.5}\,\mathrm{cm^{-2}}$ (e.g., R. Maiolino et al. 2025; V. Rusakov et al. 2026; A. Sneppen et al. 2026) have been proposed to explain the reported LRD X-ray deficit.

Testing these scenarios requires establishing both the magnitude and prevalence of the X-ray deficit. Yet even megasecond Chandra observations have so far provided weak individual constraints: only about half of broad-line LRDs have upper limits below the X-ray luminosities predicted by standard AGN relations (M. Yue et al. 2024; Q. O. Casey et al. 2026). Stacking provides stronger population-level constraints, but low-count stacks of heterogeneous samples spanning broad ranges in redshift and luminosity generally require careful interpretation. Moreover, distinguishing the physical origin of any deficit remains difficult because Chandra observations at $z \sim 6$ predominately sample rest-frame hard energies, whereas the soft X-ray in which steep intrinsic spectra and heavy obscuration differ most strongly lies below its effective bandpass.

Nearby analogs offer a direct route around this observational bottleneck. For sources of comparable intrinsic luminosity, reaching similar X-ray constraints at $z \sim 0.3$ requires $\sim 10^{3-4}$ less exposure than at $z \sim 6$, depending on the source-to-background ratio. Their proximity also reduces physical blending at a given angular resolution and, most importantly, brings the diagnostic rest-frame soft X-ray emission into the observable band.

Can we find local analogs? Well before the launch of JWST, nearby dwarf galaxies were already studied as local analogs of early galaxies (e.g., C. Simmonds et al. 2016; M. Mezcua 2017). In particular, green pea galaxies (GPs), a class of compact dwarf galaxies with strong [O III] emission, resemble high-redshift star-forming galaxies in stellar mass, size, specific star-formation rate, metallicity, and, in some cases, Lyα and LyC escape (H. Yang et al. 2016; Y. I. Izotov et al. 2016). From an initial sample of 2190 GPs, R. Lin et al. (2024) identified 59 candidates with broad emission lines indicative of AGN activity. Building on this sample, R. Lin et al. (2025) identified seven V-shaped broad-line GPs whose UV-to-optical SEDs and compact morphologies (unresolved or $\lesssim 1\,\mathrm{kpc}$ at DESI-LS10 resolution[10]) satisfy commonly used observational LRD criteria (e.g., I. Labbe et al. 2025; D. D. Kocevski et al. 2025; R. E. Hviding et al. 2025). They also resemble LRDs in their ionization conditions and apparently overmassive BHs. We therefore refer to these systems as "local little red dots" (LLRDs), without assuming a common physical origin for all LRDs. Demographically, broad-line and V-shaped broad-line systems account for 2.7% and 0.32%, respectively, of the parent GP sample. These

[10] At this resolution, their optical profiles are consistent with, or more compact than, expected from the star-forming-galaxy mass–size relation (K. V. Nedkova et al. 2021).

fractions are interestingly of the same order as the ratio of the number density of LRDs at $z \sim 6$–7 ($\sim 10^{-5}$–$10^{-4}\,\mathrm{cMpc}^{-3}$, Z. Pan et al. 2026 and references therein) to that of galaxies with $8.0 < \log(M_\star/M_\odot) < 9.5$ at similar redshifts ($\sim 3\times10^{-3}$–$4\times10^{-3}\,\mathrm{cMpc}^{-3}$, A. Weibel et al. 2024), or roughly 0.25–3%. Complementary searches have subsequently enlarged the population of candidate low-redshift LRD analogs using alternative methods (e.g., X. Lin et al. 2026a,b; X. Ji et al. 2026; W. Ding et al. 2026; P. Rinaldi et al. 2026).

Here we present a pilot X-ray study of six of the seven LLRDs identified by R. Lin et al. (2025), using pointed Einstein Probe (EP, W. Yuan et al. 2025) FXT observations obtained through our program (PI: J.-X. Wang). The remaining LLRD is excluded due to strong X-ray contamination by a DESI broad-line AGN $\sim 20''$ away. Even before considering their X-ray emission, these six LLRDs show internal diversity: J0928 and J1154 are the only two with securely detected AGN-like optical variability and also exhibit bluer optical continua than the other four objects (R. Lin et al. 2025, 2026). Although all six satisfy the original LLRD selection, these independent optical differences provide important context for interpreting their X-ray properties. We therefore ask whether this optical diversity is accompanied by a corresponding contrast in X-ray emission and what that contrast may reveal about high-redshift LRDs. Our observational results are presented in Section 2, followed by their implications for high-redshift LRDs in Section 3. Throughout this work, we adopt a cosmology with $H_0 = 67.7\,\mathrm{km\,s^{-1}\,Mpc^{-1}}$, $\Omega_\mathrm{m} = 0.31$, and $\Omega_\Lambda = 0.69$ (Planck Collaboration et al. 2020).

2. X-RAY REVEALS TWO TYPES OF LLRDS

2.1. *Direct view from EP-FXT X-ray images*

We reduce the EP-FXT data summarized in Appendix A with our custom eFXTDAS[11] tool, which extends the official FXTDAS[12] pipeline (Appendix B). Following calibration and event cleaning, we coadd the observed-frame 0.5–4 keV images from all observations and both modules and perform wavelet- and PSF-based source detection. Spectra are extracted within $60''$ (enclosing $\sim 90\,\%$ of the on-axis PSF energy), with local backgrounds from $90''$–$300''$ annuli. Contaminating sources are masked and the responses account for the resulting geometry and vignetting. From the extracted spectra, we calculate the background-only probability p_null and quote its one-sided Gaussian-equivalent significance as the source SNR (Appendix C).

As can be seen from the coadded images in Figure 1, X-ray reveals a contrast aligned with the pre-existing optical differences: J0928 and J1154 are significantly detected in X-rays, whereas J1200, J0035, J0923, and J0850 are undetected or only marginally detected despite comparable or longer exposures. We hereafter refer to these two subsets as "X-normal" and "X-weak" LLRDs, respectively.

2.2. *Benchmarking LLRD X-ray emission against local AGNs and LRDs*

To benchmark LLRDs against AGNs and high-redshift LRDs, we fit their spectra with XSPEC (K. A. Arnaud 1996) using an absorbed AGN power-law plus fixed host-galaxy emission, attenuated by Galactic absorption: `TBabs*(zTBabs`$_{\mathrm{agn}}$`*zpowerlw`$_{\mathrm{agn}}$`+host)`. For X-weak LLRDs, we adopt $N_\mathrm{H} = 10^{22}\,\mathrm{cm}^{-2}$ and $\Gamma = 1.8$, consistent with M. Yue et al. (2024), and fit only the normalization. For the X-normal LLRDs, their higher SNR allows N_H and, where warranted, the photon index to vary; J0928 additionally requires partial covering. Table 1 reports the fitted parameters; Appendix E presents details and the X-normal spectra (Figure 6). The host component includes X-ray binaries and hot gas normalized from the stellar mass and narrow-Hα-based SFR (B. D. Lehmer et al. 2010; S. Mineo et al. 2012; R. C. Kennicutt & N. J. Evans 2012; S. Liu et al. 2024). Its luminosity is only $\sim 10^{40}\,\mathrm{erg\,s^{-1}}$, and even a dex uncertainty changes the reported nuclear luminosities or upper limits by $< 5\%$.

To enhance SNR, we stack the rest-frame spectra of three X-weak LLRDs (J1200, J0035, and J0923) using XSTACK (S.-J. Chen et al. 2025), which shifts each spectrum and corresponding Galactic-N_H-corrected response to a common rest frame before combining them using average-luminosity response weighting (`LMN` mode). Here X-ray spectral stacking should be justified because the three objects span narrow ranges in redshift and broad-Hα luminosity. J0850 is excluded because its broad-Hα luminosity is ~ 1 dex lower and its shorter exposure would contribute mostly background. For comparison, the two X-normal LLRDs are stacked identically. Both results are reported in Table 1, with the X-weak stack reaching an SNR of ~ 3.5 in the rest-frame 0.5–8 keV band.

Consistent with the direct view from Figure 1, the X-weak LLRD stack is ~ 1.4–1.5 dex fainter in X-rays than the X-normal stack, although their 2500 Å and broad-Hα luminosities differ by only ~ 0.4 dex (Figure 2). The same contrast is seen relative to the unobscured type 1

[11] https://github.com/AstroChensj/eFXTDAS
[12] https://epfxt.ihep.ac.cn/analysis

Table 1. Properties of LLRDs and their stacked X-ray spectra

Name	$z_{\rm spec}$	$\log M_{\rm BH}$ ($M_\odot$)	$\log M_\star$ ($M_\odot$)	$\log {\rm SFR}$ ($M_\odot\ {\rm yr}^{-1}$)	$SF_{\infty,\rm DRW}$	$\log L_{\rm H\alpha,broad}$ (erg s^{-1})	$\log L_{2500}$ (erg s^{-1} Hz^{-1})	SNR	$\log L_{2-10}$ (erg s^{-1})	$\log L_{2\,\rm keV}$ (erg s^{-1} Hz^{-1})	$N_{\rm H}$ (10^{22} cm^{-2})	Γ	C_f
Individual sources													
J0928	0.293	7.82 ± 0.01	10.02 ± 0.04	0.65 ± 0.01	$0.18^{+0.03}_{-0.02}$	42.38 ± 0.01	28.73	13.4	$44.09^{+0.13}_{-0.13}$	$26.24^{+0.29}_{-0.32}$	$9.01^{+3.20}_{-3.27}$	$2.13^{+0.67}_{-0.71}$	$0.94^{+0.04}_{-0.13}$
J1154	0.269	7.68 ± 0.03	10.08 ± 0.10	0.26 ± 0.02	$0.18^{+0.06}_{-0.03}$	42.17 ± 0.02	28.69	6.2	$43.48^{+0.14}_{-0.15}$	$25.52^{+0.14}_{-0.15}$	$3.61^{+1.65}_{-1.19}$	1.80(∗)	1.00(∗)
J1200	0.303	8.47 ± 0.03	9.90 ± 0.03	0.74 ± 0.01	–	42.02 ± 0.02	28.36	3.0	$42.80^{+0.15}_{-0.19}$	$24.84^{+0.15}_{-0.19}$	1.00(∗)	1.80(∗)	1.00(∗)
J0035	0.242	6.60 ± 0.12	8.71 ± 0.03	0.94 ± 0.01	–	41.65 ± 0.08	28.40	2.2	< 42.82	< 24.86	1.00(∗)	1.80(∗)	1.00(∗)
J0923	0.323	6.92 ± 0.04	10.03 ± 0.20	0.52 ± 0.01	–	41.82 ± 0.03	28.34	1.5	< 42.71	< 24.75	1.00(∗)	1.80(∗)	1.00(∗)
J0850	0.280	6.33 ± 0.19	8.33 ± 0.08	0.38 ± 0.01	–	40.89 ± 0.13	28.42	0.0	< 42.94	< 24.98	1.00(∗)	1.80(∗)	1.00(∗)
Stacked spectra													
J0928+J1154	–	7.76 ± 0.01	10.05 ± 0.06	0.50 ± 0.01	–	42.29 ± 0.01	28.71	14.8	$43.92^{+0.10}_{-0.10}$	$26.10^{+0.24}_{-0.26}$	$9.34^{+2.37}_{-2.59}$	$2.22^{+0.57}_{-0.57}$	$0.95^{+0.03}_{-0.06}$
J1200+J0923+J0035	–	8.01 ± 0.03	9.81 ± 0.11	0.77 ± 0.01	–	41.86 ± 0.02	28.37	3.5	$42.55^{+0.08}_{-0.12}$	$24.59^{+0.08}_{-0.12}$	1.00(∗)	1.80(∗)	1.00(∗)

NOTE—Black-hole and stellar masses and broad Hα luminosities are from R. Lin et al. (2025), and optical-variability measurements are from R. Lin et al. (2026). SFRs are derived from $\log {\rm SFR} = \log L_{\rm H\alpha,narrow} - 41.27$ following R. C. Kennicutt & N. J. Evans (2012). L_{2500} is the interpolated, Galactic-extinction-corrected rest-frame 2500 Å monochromatic luminosity. X-ray SNRs are evaluated over the observed-frame 0.5–8 keV band for individual sources and the rest-frame 0.5–8 keV band for the spectral stacks. X-ray luminosities (2 keV monochromatic luminosity, 2–10 keV model luminosity) are absorption-corrected AGN power-law values, and $N_{\rm H}$ is the intrinsic nuclear column density. Parenthesized asterisks denote fixed parameters.

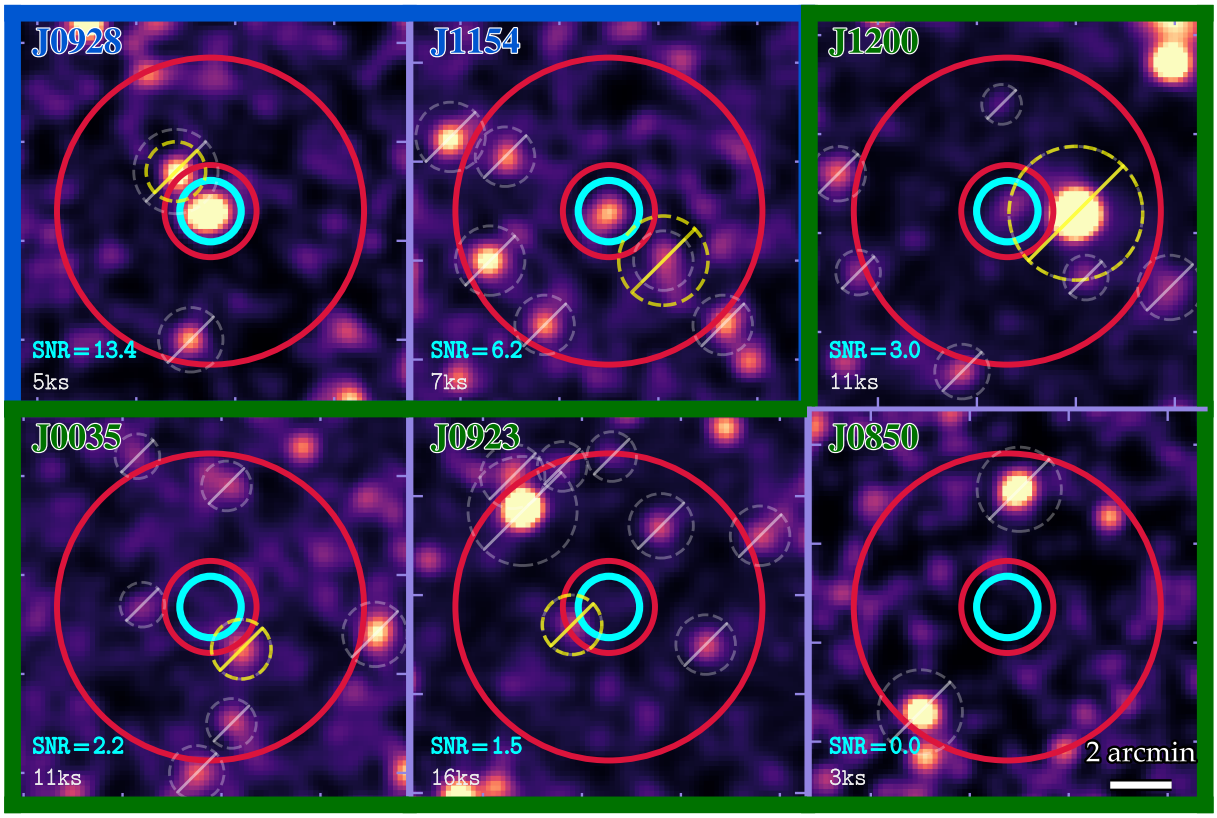


Figure 1. Observed-frame EP-FXT 0.5–4 keV exposure-corrected count-rate images, coadded over all observations and detector modules and smoothed with a Gaussian kernel of $\sigma = 2$ pixels ($\simeq 19''$). Cyan circles and crimson annuli mark the source and background apertures; yellow and gray circles show contaminant masks. Labels give the extraction-based SNR and effective exposure. Blue and green frames denote X-normal and X-weak LLRDs.

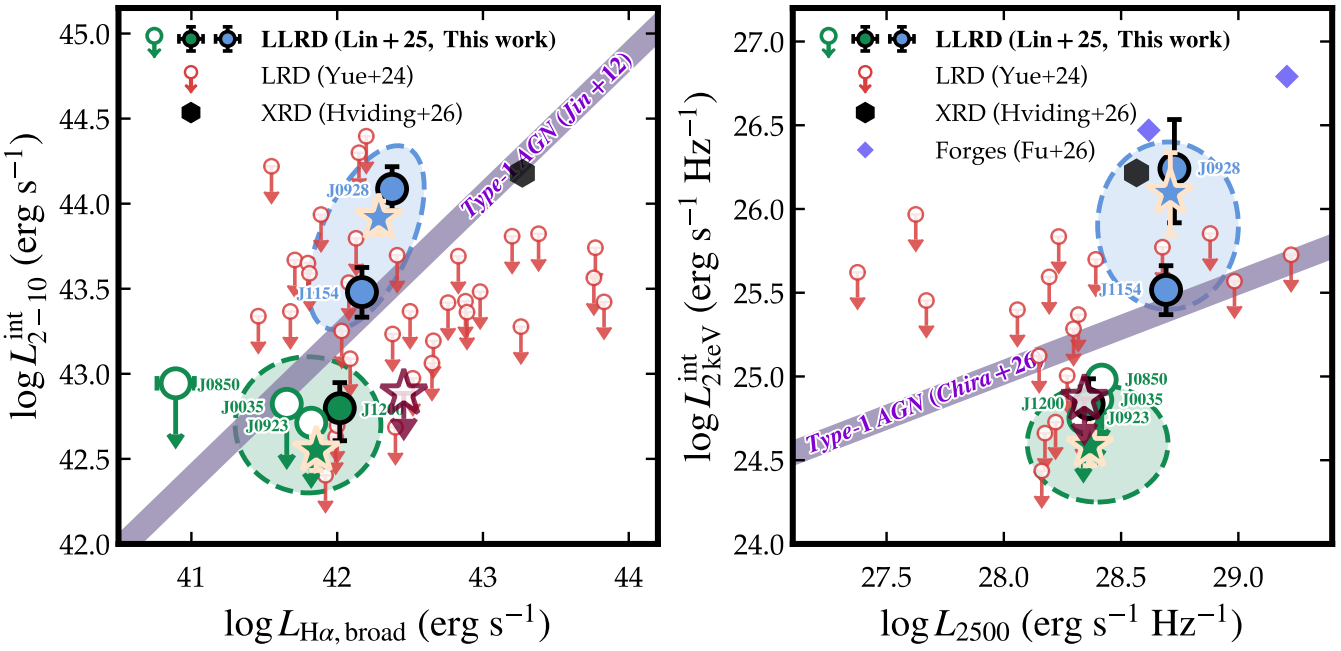


Figure 2. Intrinsic X-ray emission of LLRDs benchmarked against AGNs and high-redshift LRDs. Left: 2–10 keV luminosity versus broad-Hα luminosity; right: 2 keV monochromatic luminosity versus rest-frame 2500 Å luminosity. X-weak LLRDs are green (open circles: upper limits; filled circle: marginal J1200 detection), and X-normal LLRDs are blue; stars mark their spectral stacks, with dashed ellipses associating each stack with its members. Red circles and dark-red stars denote the individual and representative stacked 3σ LRD limits based on M. Yue et al. (2024); the stacked limits use exposure-weighted count-rate conversions and geometric-mean horizontal coordinates. Black and purple symbols show the XRD and Forges. Purple lines show the type 1 AGN relations.

AGN relations from C. Jin et al. (2012) and M. Chira et al. (2026): the marginal detection or upper limits of the individual X-weak LLRDs lie below the corresponding relations, except for J0850, whose shorter EP-FXT exposure does not provide a useful constraint in the broad-Hα comparison. The X-weak stack lies ~ 0.55 dex below the Hα-based relation and ~ 0.65 dex below the 2500 Å-based relation. By contrast, the X-normal LLRDs are consistent with or brighter than the AGN relations, with their stack lying ~ 0.6 dex above them. As a descriptive check incorporating the three individual upper limits, we also report a reverse Kaplan–Meier estimate of the six-source X-ray luminosity distribution in Appendix F.

To compare with high-redshift LRDs, Figure 2 includes the individual LRD upper limits and a representative whole-sample stacked upper limit derived from M. Yue et al. (2024). The X-weak LLRD stack lies below 95 % (19/20) of the individual limits with available L_{2500} measurements and remains compatible with the representative LRD stack. Thus, at the distance of the LLRDs, EP-FXT detects an X-ray luminosity that would remain below nearly all published individual high-redshift LRD limits, demonstrating the observational advantage of nearby analogs. For broader context, Figure 2 also shows the "X-ray dot" (XRD) and "Forges", proposed transitional objects linking LRDs to more conventional quasars (R. E. Hviding et al. 2026; S. Fu et al. 2026).

Importantly, the difference between the X-normal and X-weak LLRDs extends beyond X-rays. The two X-normal LLRDs are also the only objects with securely detected AGN-like optical variability (R. Lin et al. 2026), while X-weak LLRDs exhibit redder optical continua (Figure 3), larger mean offset from the local $M_{\rm BH}$–$M_\star$ relation (Table 1), and lack significant optical variability similar to the majority of LRDs (Z. Zhang et al. 2025). Their Balmer properties further reinforce this contrast (Figure 4; Appendix D). Joint fits to Hα, Hβ, and Hγ show that the three X-weak LLRDs in the fiducial stack have a characteristic $(\mathrm{H}\alpha/\mathrm{H}\beta)_{\rm broad}$ $\sim$7–8 or larger and an average Balmer-break strength of ~ 1.6. By contrast, X-normal LLRDs have $(\mathrm{H}\alpha/\mathrm{H}\beta)_{\rm broad} \sim 3.5$, closer to Case B recombination (2.86) and typical type 1 AGN (3.1), together with a Balmer-break strength of ~ 1.1. These coherent multi-wavelength differences motivate treating the two groups separately, with the X-weak LLRDs providing the closer local analogs for investigating the X-ray nature of high-redshift LRDs.

3. IMPLICATIONS FOR HIGH-REDSHIFT LRDS

If X-weak LLRDs trace the same physical phenomena as high-redshift LRDs, as suggested by the multiwavelength similarities discussed in Section 2.2, their proximity opens an X-ray regime otherwise inaccessible at high redshift. Indeed, with only $\sim 1/1000$ of the exposure time (~ 40 ks versus ~ 40 Ms for the LRD stack of M. Yue et al. 2024), our observations provide tighter constraints than those available for 95 % of the individual LRDs with measured L_{2500} (Figure 2).

Figure 3 compares the stacked IR–optical–UV–X-ray SEDs of the X-weak and X-normal LLRDs with the LRD SED from H. B. Akins et al. (2025). To emphasize differences in SED shape, all three are normalized at the rest-frame 2500 Å following convention in Figure 2. Remarkably, the X-weak LLRDs exhibit a prominent V-shaped optical–UV continuum closely resembling the LRD stack. The main difference occurs at rest-frame $\sim$2–3 µm, where the X-weak LLRDs are detected at a luminosity comparable to the LRD upper limit. This difference may reflect a larger contribution from an evolved stellar population in the lower-redshift galaxies (e.g., E. F. Bell & R. S. de Jong 2001; L. Bao et al. 2026).

The X-ray regime is where local analogs provide the strongest additional leverage. Figure 3 compares the observed SEDs with representative unobscured super-Eddington (K. Inayoshi et al. 2025), CT, and Compton-thin models. The intrinsic X-ray normalizations of the absorption models are tied to the average X-weak LLRD UV luminosity using the standard unobscured-quasar relation of M. Chira et al. (2026).

We derive the LLRD X-ray SEDs from response-weighted broad-band measurements normalized by the stacked L_{2500}. The X-weak stack has a $\sim 1.9\sigma$ soft-band excess, for which we adopt a 3σ upper limit, and a 3.3σ detection over 2–8 keV. Because EP-FXT effective area declines sharply above ~ 2.3 keV, the latter is weighted toward rest-frame $\sim$2–3 keV photons. By comparison, current Chandra constraints on high-redshift LRDs predominantly probe much harder rest-frame energies ($\gtrsim 6$ keV). The X-weak LLRDs therefore extend the observational view of LRD-like systems down to rest-frame energies of ~ 1 keV. The LLRD and LRD stacks differ by only $\lesssim 0.4$ dex in L_{2500}, corresponding to $\lesssim 0.2$ dex in expected normalized $L_{2\mathrm{keV}}$, making a normalized comparison possible.

The apparent hardness of the X-weak LLRD stack is in tension with the unabsorbed super-Eddington model shown in Figure 3. When normalized to the LLRD stack at 2500 Å, this very soft model, with $\Gamma \sim 3.4$, underpredicts the measured 2–3 keV luminosity by ~ 1.5 dex. At its native normalization, which is ~ 0.9 dex brighter at 2500 Å, the model remains ~ 0.6 dex below the 2–3 keV measurement while exceeding the soft-band upper limit by ~ 0.6 dex. Thus, its spectral shape cannot reproduce both constraints, and we do not favor this particular unabsorbed super-Eddington model. Nevertheless, a super-Eddington scenario with stronger X-ray normalization (e.g., C. Jin et al. 2017), modified by additional absorption (e.g., H. Liu et al. 2025; D. Kido et al. 2025; J. Liu et al. 2026; P. Madau & R. Maiolino 2026) cannot be excluded with the present data. Observations with greater sensitivity above 2 keV, for example with *XMM-Newton* and *NuSTAR*, will be required to distinguish this possibility from an intrinsically harder continuum.

Another widely discussed explanation for LRD X-ray weakness is CT obscuration, with $N_{\mathrm{H}} \gtrsim 10^{24.5}\,\mathrm{cm}^{-2}$. Assuming the intrinsic X-ray luminosity expected from local AGN relations, the CT model with a local-AGN-like geometry (J. Buchner et al. 2019) is compatible with the very-hard-X-ray LRD upper limits but underpredicts the X-weak LLRD luminosity around 2–3 keV by more than 2 dex. The measured X-weak LLRD L^{int}_{2-10} is ~ 27 % of that predicted from the broad-Hα luminosity using the C. Jin et al. (2012) relation.

Additional soft X-ray emission scattered by a warm ionized medium could partially alleviate this tension. Such a component may be relevant given the strong [O III] emission, with average EWs of $\sim$300–400 Å, observed in both LRDs (e.g., A. de Graaff et al. 2025; Z. Ji et al. 2026) and LLRDs. However, the relation measured for local obscured AGNs by K. K. Gupta et al. (2021) gives a conservative upper estimate of only $\sim 5.6 \pm 1.5\%$ for the scattering fraction at the average LLRD $L_{[\mathrm{O\,III}]}/L^{\mathrm{int}}_{2-10\,\mathrm{keV}}$. Adopting a larger intrinsic $L^{\mathrm{int}}_{2-10\,\mathrm{keV}}$ (i.e., $N_{\mathrm{H}} > 10^{22}\,\mathrm{cm}^{-2}$) would reduce this expected fraction even further. A separate possibility is that lower metallicity weakens photoelectric absorption, as potentially motivated by the dust-poor nature of LRDs (e.g., K. Chen et al. 2025; D. J. Setton et al. 2025) and LLRDs. However, even in the limiting metal-free case, attenuation of the direct beam by Compton scattering alone gives a maximum transmission of $e^{-\tau_{\mathrm{T}}} = e^{-N_{\mathrm{H}}\sigma_{\mathrm{T}}} \simeq 12\,\%$ at $N_{\mathrm{H}} = 10^{24.5}\,\mathrm{cm}^{-2}$. Combining this limiting direct transmission (12 %) with the conservatively estimated scattered component ($\lesssim 5$ %) still falls below the observed value of 27 %. Thus, although the present data do not formally exclude CT obscuration, they are difficult to reconcile with the adopted CT model unless LLRDs have substantially stronger scattering, more prominent low-column-density leakage, or a different obscuring geometry from typical local obscured AGNs.

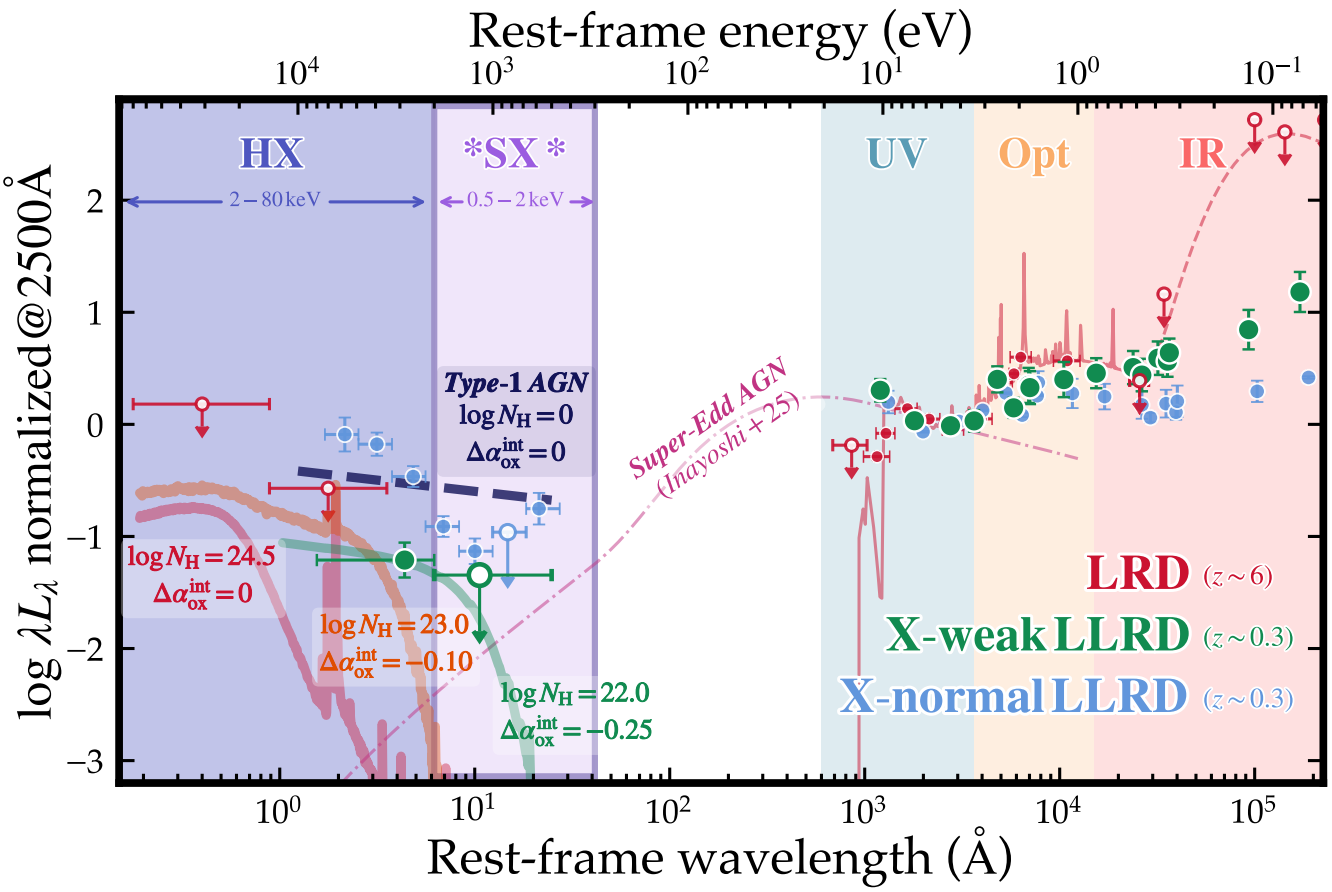


Figure 3. Normalized IR–optical–UV–X-ray SEDs of the X-weak LLRDs (green), X-normal LLRDs (blue), and high-redshift LRDs (red). All SEDs are normalized at the rest-frame 2500 Å. The LLRD measurements combine EP-FXT X-ray spectroscopy with GALEX, SDSS, SPHEREx, and WISE photometry. The red measurements and background SED model show the stacked LRD constraints from H. B. Akins et al. (2025). The curves show a typical unobscured super-Eddington model with $\dot{m} = 1$ and $M_{\rm BH} = 10^7\,M_\odot$ (K. Inayoshi et al. 2025); a CT model with $N_{\rm H} = 10^{24.5}\,{\rm cm}^{-2}$ and $\Delta\alpha_{\rm ox} = 0$; a Compton-thin model with $N_{\rm H} = 10^{23}\,{\rm cm}^{-2}$ and $\Delta\alpha_{\rm ox} = -0.10$; the fitted X-weak LLRD model with $N_{\rm H} = 10^{22}\,{\rm cm}^{-2}$ and $\Delta\alpha_{\rm ox} = -0.25$; and an unabsorbed local-AGN model with $\Delta\alpha_{\rm ox} = 0$.

Importantly, the X-weak LLRDs show that a system satisfying the observational LRD criteria—with a compact morphology, broad Hα, and a V-shaped continuum—does not necessarily require extreme X-ray weakness. Most individual high-redshift LRD limits remain too shallow to establish the magnitude of their X-ray deficits; indeed, Q. O. Casey et al. (2026) showed that X-ray-detected local LRD-like quasars and ordinary quasars would frequently remain undetected under the published LRD limits. Our X-weak LLRD stack shows a moderate deficit of ~ 0.65 dex relative to the standard $L_{\rm 2keV}^{\rm int}$–L_{2500} relation, yet remains compatible with both the representative LRD stack and 95 % of the individual LRD upper limits. Current measurements therefore permit many LRDs to have similarly moderate deficits and do not require extreme X-ray weakness to be universal. Such a moderate deficit is close to the conventional threshold used to classify X-ray-weak AGNs (e.g., Q. Ni et al. 2018) and is not surprising among local broad-line dwarf galaxies (e.g., R. Dong et al. 2012; P. G. Boorman et al. 2025), within a broader low-mass AGN population spanning a wide range of specific accretion rates (Z. Igo et al. 2026). A Compton-thin absorber with $N_{\rm H} \sim 10^{22-23}\,{\rm cm}^{-2}$, combined with a mildly weak corona with $\Delta\alpha_{\rm ox} \sim -0.1$ to -0.2, is sufficient to reproduce the X-weak LLRD measurements without invoking more extreme scenarios. Physically, this may arise from a less extended corona, so that a smaller fraction of the accretion power is dissipated in hot electrons and emitted as Comptonized X-rays (e.g., C. Done et al. 2012; A. Kubota & C. Done 2018; S. Hagen et al. 2024; S.-J. Chen et al. 2025).

The Balmer diagnostics provide an independent view of this absorbing medium. Figure 4 compares the LL-

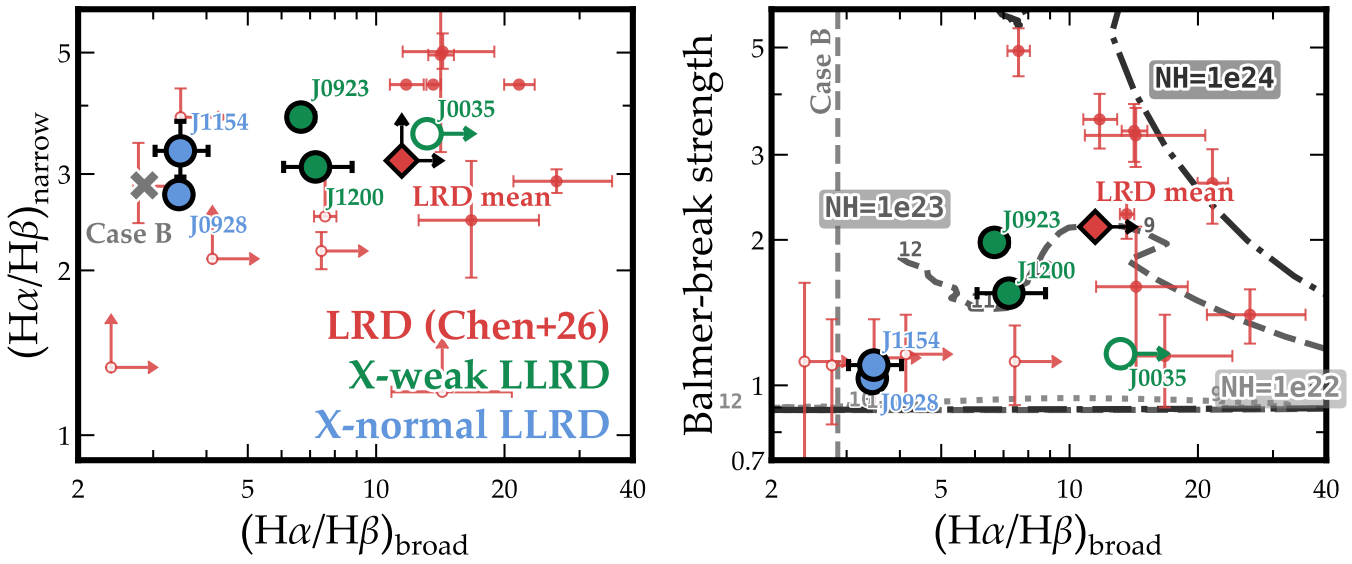


Figure 4. Balmer diagnostics support X-normal/weak division and moderate ($N_{\rm H} \sim 10^{22-23}\,{\rm cm}^{-2}$) obscuration of X-weak LLRDs. Left: broad versus narrow Hα/Hβ. Right: Balmer-break strength versus broad Hα/Hβ. Red, green, and blue symbols denote LRDs from C.-H. Chen et al. (2026), X-weak LLRDs, and X-normal LLRDs, respectively. Arrows indicate limits, diamonds mark representative LRD average, and gray symbols indicate Case B. Curves in the right panel show the dense-gas calculation from Z. Yan et al. (2026): boxed labels identify $N_{\rm H}$ for each track, while numbers along the tracks give $n_{\rm H}$ in logarithm cm^{-3}.

RDs with high-redshift LRDs from C.-H. Chen et al. (2026) and the dense-gas calculations of Z. Yan et al. (2026). Despite lacking obvious Balmer absorption, the X-weak LLRDs show elevated broad-line decrements and stronger Balmer breaks in the same direction as the high-redshift LRDs, while the X-normal LLRDs lie closer to type 1 AGNs. Within the Z. Yan et al. (2026) calculations, the X-weak LLRD average favors $n_{\rm H} \sim 10^{9-11}\,{\rm cm}^{-3}$ and $N_{\rm H} \sim 10^{22-23}\,{\rm cm}^{-2}$, independently consistent with the moderate obscuration favored by the stacked X-ray SED. J0923 lies between $N_{\rm H} \sim 10^{23}\,{\rm cm}^{-2}$ and $10^{24}\,{\rm cm}^{-2}$ tracks while remaining undetected in X-rays, suggesting a comparatively larger column to be investigated in the future. Together, the progression from high-redshift LRDs through X-weak to X-normal LLRDs/type 1 AGNs motivates a possible sequence where the central engine becomes increasingly exposed.

Finally, other local-analog searches provide a useful comparison. Q. O. Casey et al. 2026 selected LRD-like colors from SDSS low-redshift quasars, rather than starting with dwarf galaxies, and found that many such quasars would remain undetected under the published high-redshift LRD X-ray limits. Despite the different selections, their result and ours agree that LRD-like appearance and individual high-redshift X-ray non-detections do not, by themselves, require an extreme X-ray deficit. Our X-weak LLRDs additionally suggest a connection between X-ray weakness and the nuclear gas traced by the Balmer decrement and break. At a more X-ray faint extreme, the local analog known as *the Egg* (X. Lin et al. 2026a) shows the prominent Balmer absorption and break and a much stronger X-ray deficit relative to ordinary AGNs (C. Simmonds et al. 2016). Its non-detection is compatible with CT obscuration if its intrinsic X-ray emission resembles that of a standard AGN (X. Ji et al. 2026). These different local samples motivate testing whether Balmer diagnostics track X-ray emergence across the growing population of LRD local analogs (e.g., X. Lin et al. 2026b; W. Ding et al. 2026; P. Rinaldi et al. 2026).

4. SUMMARY AND FUTURE PROSPECTS

Targeted EP-FXT observations of six LLRDs demonstrate how local analogs can bypass the high-redshift LRD X-ray bottleneck. Using $\sim 1/1000$ of the exposure for current LRD stacks, we obtain constraints tighter than those available for 95 % of individual LRDs with measured L_{2500} while directly probing rest-frame soft X-rays inaccessible to Chandra at $z \sim 6$.

The observations reveal two X-ray classes. Two X-normal LLRDs exhibit normal to moderately enhanced X-ray emission, optical variability, and bluer optical continua. The X-weak subset, which most closely resembles high-redshift LRDs in optical/UV SED shape, Balmer diagnostics, and lack of detected variability, lies ~ 0.65 dex below the standard unobscured-quasar $L^{\rm int}_{\rm 2keV}$–L_{2500} relation. Stacking three X-weak LLRDs

yields a 3.3σ detection in the rest-frame 2–8 keV band, driven mainly by 2–3 keV photons. The rest-frame 0.5–2 keV band is not significantly detected (1.9σ). The moderate deficit measured from the X-weak LLRD stack remains compatible with current individual and stacked LRD constraints, showing that extreme X-ray weakness need not be universal.

The rest-frame soft-X-ray constraints are difficult to reconcile with either the typical unobscured super-Eddington model or the local-AGN-like CT geometry examined here, although absorbed super-Eddington spectra with stronger intrinsic X-ray emission, or CT configurations with substantially enhanced scattering or low-column-density leakage cannot be excluded. The simplest explanation consistent with both the X-ray and Balmer diagnostics is a mildly X-ray-weak corona, with $\Delta\alpha_{\rm ox} \sim -0.1$ to -0.2, viewed through Compton-thin material with $N_{\rm H} \sim 10^{22-23}\,{\rm cm}^{-2}$. Deeper X-ray observations and growing samples of local LRD analogs will test whether this interpretation is representative and clarify the diversity and physical origin of LRD X-ray emission beyond what is currently feasible at high redshift.

ACKNOWLEDGMENTS

This work was supported by the National Natural Science Foundation of China (grant nos. 12533006, 12192221, 12373016, 123B2042), and Guizhou Provincial Major Scientific and Technological Program XKBF (2025)010 and XKBF (2025)011. ZYZ acknowledges the support of the Shanghai Leading Talent Program of Eastern Talent Plan (LJ2025051) and the China-Chile Joint Research Fund 178GJHZ2025067MI. LCH was supported by the China Manned Space Program (CMS-CSST-2025-A09), the National Science Foundation of China (12233001), and the National Key R&D Program of China (2022YFF0503401). ZI acknowledges support through the European Space Agency (ESA) Research Fellowship in Space Science.

We thank the referee and editors for their helpful comments that improved the manuscript. We thank Shouyi Wang for discussions on EFXTDAS and technical aspects of EP-FXT, Shuying Zhou for scientific discussion during the CSST annual meeting. We also acknowledge R. E. Hviding et al. (2026), whose compilation we digitized to obtain the comparison data points from M. Yue et al. (2024), S. Fu et al. (2026), and R. E. Hviding et al. (2026) shown in Figure 2.

This work uses the GALEX UV Unique Source Catalog (GUVcat) AIS (P. Morrissey et al. 2007; L. Bianchi et al. 2017; L. Bianchi 2020; L. Bianchi & B. Shiao 2020), hosted by the Mikulski Archive for Space Telescopes (MAST). The GUVcat data used in this work are available at https://doi.org/10.17909/T9-PYXY-KG53. MAST is hosted by the Space Telescope Science Institute, which is operated by the Association of Universities for Research in Astronomy, Inc., under NASA contract NAS 5–26555.

This work also uses the AllWISE Source Catalog (E. L. Wright et al. 2010; AllWISE Team 2019) and SPHEREx Quick Release 2 spectral images (J. J. Bock et al. 2026; Spherex Team 2025), hosted by the NASA/IPAC Infrared Science Archive (IRSA). IRSA is funded by the National Aeronautics and Space Administration and operated by the California Institute of Technology. This publication makes use of data products from the Wide-field Infrared Survey Explorer, a joint project of the University of California, Los Angeles, and the Jet Propulsion Laboratory/California Institute of Technology, funded by NASA. This publication also makes use of data products from SPHEREx, a joint project of the Jet Propulsion Laboratory and the California Institute of Technology, funded by NASA.

Funding for the Sloan Digital Sky Survey IV has been provided by the Alfred P. Sloan Foundation, the U.S. Department of Energy Office of Science, and the Participating Institutions. SDSS acknowledges support and resources from the Center for High-Performance Computing at the University of Utah. The SDSS website is https://www.sdss4.org.

SDSS is managed by the Astrophysical Research Consortium for the Participating Institutions of the SDSS Collaboration, including the Brazilian Participation Group, the Carnegie Institution for Science, Carnegie Mellon University, Center for Astrophysics | Harvard & Smithsonian (CfA), the Chilean Participation Group, the French Participation Group, Instituto de Astrofísica de Canarias, The Johns Hopkins University, Kavli Institute for the Physics and Mathematics of the Universe (IPMU) / University of Tokyo, the Korean Participation Group, Lawrence Berkeley National Laboratory, Leibniz-Institut für Astrophysik Potsdam (AIP), Max-Planck-Institut für Astronomie (MPIA Heidelberg), Max-Planck-Institut für Astrophysik (MPA Garching), Max-Planck-Institut für Extraterrestrische Physik (MPE), National Astronomical Observatories of China, New Mexico State University, New York University, University of Notre Dame, Observatório Nacional / MCTI, The Ohio State University, Pennsylvania State University, Shanghai Astronomical Observatory, United Kingdom Participation Group, Universidad Nacional Autónoma de México, University of Arizona, University of Colorado Boulder, University of Oxford,

Table 2. Einstein Probe/FXT observation summary for the LLRDs

Name	R.A. (deg)	Decl. (deg)	ObsID	Observing span (UTC)	Exposure (ks)	Mode
J092834.85+292136.3	142.1452	29.3601	11900576513, 11900576514 11900576517, 11900594305	2026-01-29–2026-02-07	5.3	FF 01
J115438.96+065025.0	178.6624	6.8403	11900528385, 11900545668 11900574849, 11900574850 11900574851	2025-12-26–2026-01-28	7.2	FF 01
J120052.37+331238.4	180.2182	33.2107	11900712450, 11900712451 11900712452, 11900712453 11900712454, 11900712455 11900712456, 11900712457 11900712458, 11900712459 11900719745, 11900719747 11900719749	2026-05-03–2026-05-10	11.3	FF 01
J003515.16+084859.9	8.8132	8.8167	11900458113, 11900458117 11900458118, 11900458119 11900465410, 11900465411 11900465412, 11900465414 11900465415, 11900512001 11900512002, 11900512003	2025-11-01–2025-12-13	11.1	FF 01
J092359.89+415736.7	140.9995	41.9602	11900610563, 11900610567 11900610569, 11900618244 11900618245, 11900618246 11900618497, 11900618498 11900618499, 11900618501 11900674177, 11900674178 11900674179	2026-02-19–2026-04-06	15.7	FF 01
J085058.09+303053.6	132.7421	30.5149	11900638728, 11900638729 11900638730, 11900638732 11900638733, 11900638734	2026-03-11–2026-03-12	3.4	FF 01

NOTE—Dates are given in UTC. The exposure is the module-averaged value, $(t_{\rm FXTA}+t_{\rm FXTB})/2$, summed over the listed ObsIDs; it therefore represents the effective on-source exposure rather than the module-summed collecting time. "FF" and "01" denote the full-frame observing mode and thin-filter configuration, respectively.

University of Portsmouth, University of Utah, University of Virginia, University of Washington, University of Wisconsin, Vanderbilt University, and Yale University.

This work made use of data from LAMOST (the Large Sky Area Multi-Object Fiber Spectroscopic Telescope, also known as the Guoshoujing Telescope; https://cstr.cn/31118.02.LAMOST; X.-Q. Cui et al. 2012). LAMOST is a Chinese national mega-science facility operated by the National Astronomical Observatories, Chinese Academy of Sciences.

Facilities: EP-FXT, GALEX, SDSS, SPHEREx, WISE

Software: HEAsoft (v6.28; HEASARC 2014), XSPEC (K. A. Arnaud 1996), TOPCAT (M. B. Taylor 2005), GNU Parallel Tool (O. Tange 2011), FXTDAS v1.30 (https://epfxt.ihep.ac.cn/analysis), eFXTDAS (https://github.com/AstroChensj/eFXTDAS), XSTACK (https://github.com/AstroChensj/Xstack)

APPENDIX

A. LLRD EP-FXT OBSERVATION SUMMARY

Table 2 summarizes the pointed EP-FXT observations obtained through our program (PI: J.-X. Wang) for the six LLRDs analyzed in this work. The exposure times were planned to yield at least a 3σ detection for an intrinsic 2–10 keV luminosity 0.5 dex below that expected from the standard broad-Hα AGN relation. J0850 was assigned a

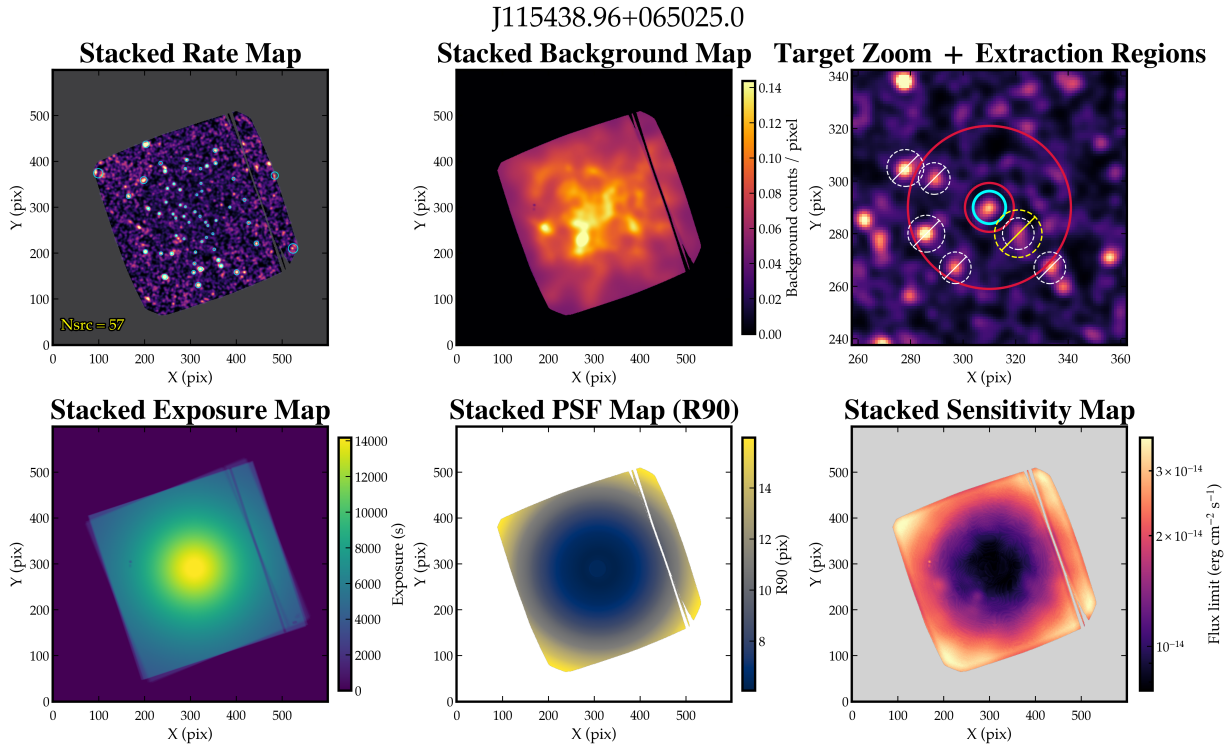


Figure 5. Example eFXTDAS quality-assessment summary for J115438.96+065025.0, generated with `fxtcombine-quickview`. From upper left to lower right, the panels show the stacked count-rate map and detected-source catalog, modeled background map, target-centered extraction geometry (overlaid with contaminating sources in the source/background extraction regions), stacked exposure map, 90%-encircled-energy PSF-radius map, and limiting-flux sensitivity map.

shorter exposure because its broad-Hα luminosity is approximately 1 dex lower than those of the other targets; for this source, the observational goal was to improve upon the archival eROSITA upper limit rather than to secure an individual detection.

B. eFXTDAS: ENHANCED DATA ANALYSIS TOOLS FOR EP-FXT

The official FXTDAS software (version 1.30; CALDB version 1.30) provides the basic calibration and event-cleaning workflow for individual EP-FXT observations. Scientific analysis nevertheless requires additional capabilities, including source detection, contaminant-aware region construction, response generation for non-trivial extraction geometries, and the combination of imaging and spectral products from multiple observations and detector modules. We developed eFXTDAS to provide these capabilities and orchestrate the official tasks within a reproducible end-to-end workflow. The software is publicly available at https://github.com/AstroChensj/eFXTDAS; its top-level task, `fxtcombine`, performs the following steps.

1. *Calibration and preparation of individual observations.* During the first iteration over the observations, `fxtcombine` processes each OBSID and FXT module separately. It invokes the official FXTDAS tasks for coordinate reconstruction, energy calibration, particle identification, bad-pixel filtering, event grading, and construction of the basic good-time intervals. For observations obtained in full-frame mode, the corresponding `fsaevt` data are used to identify periods of enhanced instrumental background. The `fxtbkgoptrate` task derives an optimized background-rate threshold from the `fsaevt` light curve (defaults to `robust_iqr.`), and the resulting flare-filtered good-time intervals are applied consistently to both the `fsaevt` and science event files.

   The cleaned science events are then used to extract the 0.5–4 keV[13] counts image and to generate the corresponding vignetting-corrected exposure map. For each observation, `fxtpsfgen` also evaluates the calibrated energy-

[13] This energy range is chosen for visualization and later source detection, because it maximizes the source-to-background ratio: the EP-FXT effective area declines while the instrumental background becomes increasingly important at higher energies. By contrast, the extraction-based significance quoted in main text and Appendix C is evaluated over 0.5–8 keV, retaining the full calibrated spectral band.

and off-axis-angle-dependent PSF and stores it as an observation PSF product containing the local encircled-energy-fraction curves. These per-observation images, exposure maps, and PSF products form the inputs to the subsequent stacking analysis.

2. *Image and PSF stacking.* For each target, the cleaned events from all OBSIDs and both FXT modules are reprojected onto a common celestial frame and accumulated to form the stacked counts image. The corresponding exposure maps are reprojected and summed on the same grid. An exposure-corrected count-rate map is then obtained by dividing the stacked counts map by the stacked exposure map; this rate map is used primarily for visualization.

   The effective PSF of the stacked observation is constructed from the individual observation PSF products. At each position in the stacked image, the local encircled-energy curves from the contributing observations are averaged using their reprojected exposure values as weights. The radius enclosing a requested fraction of the source counts, such as the 90% encircled-energy radius, is then obtained by inverting this exposure-weighted stacked curve. This procedure accounts for the different off-axis angles and exposure contributions of the individual observations.

3. *Source detection.* Source detection is performed with `fxtsrcdet` on the stacked 0.5–4 keV counts image, using the stacked exposure map and PSF product. A multiscale Mexican-hat wavelet search first identifies provisional source candidates. Significant candidate regions are temporarily carved from the image, and the remaining counts are adaptively smoothed relative to the exposure map to construct the background model. The candidate list is then refined through PSF-based Cash-statistic fitting. Sources sufficiently close for their PSFs to overlap are fitted simultaneously to reduce source confusion and flux cross-contamination.

   For a point-source candidate, `fxtsrcdet` compares the best-fitting source-plus-background model with the background-only model and defines

$$\texttt{DETLIKE} = -\ln p, \qquad p = Q\left(\frac{3}{2}, \frac{\Delta C}{2}\right), \tag{B1}$$

   where ΔC is the improvement in the Cash statistic and Q is the regularized upper incomplete gamma function[14]. The three effective degrees of freedom correspond to the source amplitude and two centroid coordinates. Candidates with $\texttt{DETLIKE} > 6$ are retained in the clean source catalog, following a conventional threshold used in eROSITA-like source detection (T. Liu et al. 2022)[15]. This image-fitting likelihood is distinct from the extraction-based SNR defined in Equation C5.

4. *Construction of extraction regions.* The `fxtregions` task matches the source catalog to the optical target position within 8.6″, corresponding approximately to the 90 %-confidence FXT positional accuracy, including systematic uncertainty (EP Science Center 2024). When a counterpart is identified, the fitted X-ray centroid is adopted as the extraction center; otherwise, the optical position is used.

   For the present analysis, `fxtregions` creates a circular source region of radius 60″, enclosing $\sim$ 90 % of the on-axis PSF energy, and a background annulus spanning 90″–300″. Neighboring sources are excised from the source and background regions with circular masks whose radii are determined from their fitted PSF profiles. Within the background annulus, each mask extends to the radius at which the contaminant surface brightness falls below 10% of the local background. If a contaminant overlaps the source aperture, its mask instead extends to the radius at which its surface brightness falls below 20% of the modeled target surface brightness. For an undetected target, for which the latter quantity cannot be constrained, the background-based criterion is used instead.

5. *Spectral extraction and response generation.* After the regions have been established from the stacked image, `fxtcombine` performs a second iteration over all OBSIDs and detector modules. Source and background spectra are extracted separately from each cleaned event file using the same sky regions. The corresponding ARF and RMF are generated with `fxtrspgen`.

[14] See also https://erosita.mpe.mpg.de/dr1/eSASS4DR1/eSASS4DR1_tasks/ersensmap_doc.html.

[15] As per eROSITA simulations (R. Seppi et al. 2022), this threshold corresponds roughly to 14 % false positive rate.

The standard FXTDAS `fxtarfgen` task does not account for a compound source aperture consisting of a positive region with one or more subtracted contaminant regions. Such a source-source collision case should be common especially in deep exposures, given the relative broad PSF of EP-FXT. In our custom `fxtrspgen` task, we rasterize the complete DS9 region expression and calculates the response for the retained aperture. The extracted ARF includes the spatially weighted vignetting correction, the energy-dependent PSF fraction enclosed by the aperture, and the fractional region coverage on the exposure map. The response therefore remains consistent with the source spectrum even when part of the nominal circular aperture has been removed.

6. *Spectral stacking and diagnostic products.* Finally, the source and background PI spectra and their associated responses from the individual observations and detector modules are combined in observed-frame using XSTACK in its `same-target` mode. The source and background counts are summed directly, while the full response matrices (ARF × RMF) are combined with exposure weighting and normalized by the total exposure before being decomposed into the stacked ARF and RMF. The stacked `EXPOSURE` is the sum of the individual exposures, whereas `AREASCAL`, `BACKSCAL`, and `CORRSCAL` are assigned their respective arithmetic means, separately for the source and background spectra. This produces a single stacked source spectrum and associated background and response files for each target, with a response representing the exposure-weighted contributions of the individual observations.

   For the convenience of users, `fxtcombine` also generates a sensitivity map from the stacked background, exposure, and PSF products. At each image position, the task calculates the limiting source flux for the adopted encircled-energy aperture and detection-likelihood threshold. The complete set of imaging and diagnostic products is collected by `fxtcombine-quickview` into the summary shown in Figure 5. This combined view allows the stacked rate, background, exposure, PSF, sensitivity, and extraction-region products to be inspected together before the final spectra are analyzed.

C. EXTRACTION-BASED DETECTION SIGNIFICANCE

For a chosen energy band, we sum the source-aperture counts to obtain S and the background-spectrum counts to obtain B. The background uncertainty σ_B is obtained by adding the channel-level `STAT_ERR` values in quadrature. The background-to-source scaling factor is

$$\alpha = \frac{\texttt{EXPOSURE}_{\rm src}}{\texttt{EXPOSURE}_{\rm bkg}} \frac{\texttt{BACKSCAL}_{\rm src}}{\texttt{BACKSCAL}_{\rm bkg}} \frac{\texttt{AREASCAL}_{\rm src}}{\texttt{AREASCAL}_{\rm bkg}}, \tag{C2}$$

where `EXPOSURE`, `BACKSCAL`, `AREASCAL` are standard OGIP keywords.

Under the background-only hypothesis, the expected source-aperture counts are αb, where $b \geq 0$ is the unknown true background level corresponding to the background spectrum. We treat $B \pm \sigma_B$ as a Gaussian measurement of b and adopt a flat prior over $b \geq 0$. The marginalized background-only probability is then

$$P_{\rm Pois}(N \geq S \mid \alpha b) = \sum_{n=S}^{\infty} \frac{\exp(-\alpha b)(\alpha b)^n}{n!}, \tag{C3}$$

and

$$p_{\rm null} = \frac{\displaystyle\int_0^{\infty} P_{\rm Pois}(N \geq S \mid \alpha b) \exp\left[-\frac{(b-B)^2}{2\sigma_B^2}\right] {\rm d}b}{\displaystyle\int_0^{\infty} \exp\left[-\frac{(b-B)^2}{2\sigma_B^2}\right] {\rm d}b}. \tag{C4}$$

We convert this probability to a one-sided Gaussian-equivalent significance,

$$\mathrm{SNR} = \max\left[0, \Phi^{-1}(1 - p_{\rm null})\right], \tag{C5}$$

where Φ is the standard-normal cumulative distribution function. Values with $p_{\rm null} > 0.5$ are reported as zero significance. This aperture-based statistic is distinct from the image-based `DETLIKE`, which is derived from PSF fitting.

Table 3. Balmer-line ratios and Balmer-break strengths of the LLRDs

X-ray class	Name	Hα/Hβ		Hγ/Hα		Balmer-break strength
		Narrow	Broad	Narrow	Broad	
X-normal	J0928	$2.75^{+0.10}_{-0.10}$	$3.45^{+0.11}_{-0.10}$	$0.161^{+0.008}_{-0.008}$	$0.117^{+0.009}_{-0.009}$	1.033 ± 0.006
X-normal	J1154	$3.31^{+0.44}_{-0.35}$	$3.47^{+0.56}_{-0.44}$	$0.156^{+0.037}_{-0.037}$	< 0.276	1.101 ± 0.048
X-weak	J1200	$3.09^{+0.08}_{-0.07}$	$7.21^{+1.58}_{-1.14}$	$0.141^{+0.005}_{-0.005}$	< 0.169	1.551 ± 0.016
X-weak	J0035	$3.55^{+0.06}_{-0.06}$	> 13.16	$0.120^{+0.003}_{-0.003}$	< 0.035	1.163 ± 0.024
X-weak	J0923	$3.81^{+0.16}_{-0.15}$	$6.66^{+0.51}_{-0.46}$	$0.117^{+0.009}_{-0.009}$	$0.068^{+0.011}_{-0.010}$	1.976 ± 0.046
X-weak	J0850	$2.44^{+0.15}_{-0.13}$	–	$0.271^{+0.022}_{-0.022}$	–	0.794 ± 0.042

NOTE—The X-ray classes follow the grouping adopted in the main analysis. All ratios and break strengths are corrected for Galactic extinction but not for attenuation internal to the sources. Errors on measured line ratios are 16th–84th percentile intervals from the joint posterior; "<" and ">" denote one-sided Gaussian-equivalent 3σ limits (the 99.865th or 0.135th posterior percentile). Dashes mark undefined broad ratios when broad Hα itself is not significantly detected. Break errors are propagated statistical errors. The break is defined by Equation D6.

D. BALMER DECREMENT/BREAK MEASUREMENTS

We measured the Balmer-line ratios uniformly from the original SDSS/LAMOST spectra rather than combining the independently fitted catalog fluxes from R. Lin et al. (2025). After correcting each rest-frame spectrum for Galactic extinction with the SFD reddening map and an $R_V = 3.1$ law (E. L. Fitzpatrick 1999), we determined the stellar continuum and Balmer absorption with pPXF and E-MILES templates (M. Cappellari 2017). The Balmer emission regions were masked during this step. pPXF freely determined the mixture of stellar templates and their velocity shift and broadening, while an additive polynomial absorbed smooth continuum-shape and calibration residuals. We repeated the continuum fit over a modest range of polynomial orders, adopted the median prediction, and included their scatter in the line-spectrum uncertainty. The adopted stellar-continuum model was then subtracted from the spectrum before the emission-line analysis, in which only a local linear residual continuum was allowed to vary within each fitting window.

We jointly fitted the Hγ (4260–4430 Å), Hβ (4750–5105 Å), and Hα (6450–6800 Å) windows. The six narrow and broad Balmer fluxes were independently free and nonnegative. Given the limited spectral quality, the three narrow lines shared one free velocity and width, and the three broad lines shared a separate free velocity and width. The fit also included the neighboring [O III], [N II], and [S II] emission. Their principal amplitudes were free, while the [O III] and [N II] doublet ratios were fixed to their theoretical values. Narrow neighboring lines shared the narrow Balmer kinematics. Additional wide [O III] and Hα components had free amplitudes and fixed kinematics. All profiles included instrumental broadening assuming resolving power $R = 1800$.

Line ratios are evaluated for each joint-posterior sample, thereby retaining covariance between the shared profiles. We report posterior medians and 16th–84th percentile intervals for detections, and one-sided 3σ limits otherwise (Table 3). J0923 has $(\mathrm{H}\alpha/\mathrm{H}\beta)_{\mathrm{broad}} = 6.66^{+0.51}_{-0.46}$ and $(\mathrm{H}\gamma/\mathrm{H}\alpha)_{\mathrm{broad}} = 0.068^{+0.011}_{-0.010}$. For J0035, the nondetections of broad Hβ and Hγ instead give $(\mathrm{H}\alpha/\mathrm{H}\beta)_{\mathrm{broad}} > 13.16$ and $(\mathrm{H}\gamma/\mathrm{H}\alpha)_{\mathrm{broad}} < 0.035$.

Independently of the line fit, we measured the Balmer break directly from the original, continuum-included spectrum. No pPXF continuum model or emission-line model enters this measurement. We define

$$\text{Balmer-break strength} \equiv \frac{\langle f_\nu \rangle_{4000-4500\,\text{Å}}}{\langle f_\nu \rangle_{3000-3500\,\text{Å}}}, \tag{D6}$$

where each mean is a wavelength-integrated mean flux density per unit frequency. J0923 has the strongest local break, 1.976 ± 0.046, whereas J0035 has only 1.163 ± 0.024 despite its more extreme line-ratio limits. The two diagnostics therefore need not vary together source by source. Interestingly, J0923 also has a radio counterpart with reported variability (T. An et al. 2026), potentially tracing jet- or wind-driven shocks in its gas-rich nuclear environment. A detailed joint radio/X-ray investigation is deferred to future work.

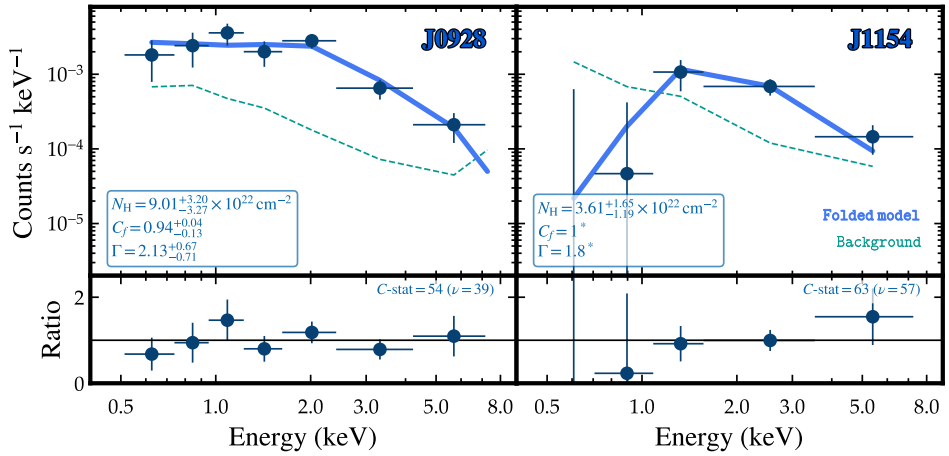


Figure 6. Observed-frame 0.5–8 keV EP-FXT spectra of the X-normal LLRDs J0928 (left) and J1154 (right). Upper panels show the spectra, response-folded best-fitting models, and expected backgrounds; lower panels show the data-to-model ratios.

E. SPECTRAL-FITTING DETAILS AND THE X-NORMAL LLRDS

The spectral models and stacking procedure are described in Section 2.2. Here we provide additional fitting details and present the spectra of the two X-normal LLRDs.

Individual spectra are grouped to contain at least five background counts per bin and fitted over the observed-frame 0.5–8 keV band using the C-statistic (J. Buchner & P. Boorman 2023). The higher-count stacked spectra are fitted over the rest-frame 0.5–8 keV band using the PG-statistic (S.-J. Chen et al. 2025). We use $\Delta C = 1$ to determine the quoted 1σ luminosity and parameter uncertainties for detected sources, and $\Delta C = 9$ to derive the 3σ luminosity upper limits for nondetections.

The fixed host component in Section 2.2 is $\texttt{zTBabs}_{\rm host}\texttt{*(zpowerlw}_{\rm xrb}\texttt{+mekal)}$. We adopt $N_{\rm H,host} = 10^{21}$ cm^{-2} and $\Gamma_{\rm xrb} = 1.8$, and normalize the X-ray-binary component from the stellar mass and SFR following B. D. Lehmer et al. (2010). The `mekal` component has $kT = 0.24$ keV and is normalized from the SFR following S. Mineo et al. (2012). As noted in the main text, these host components are negligible at the present sensitivity.

For J1154, the photon index is fixed at $\Gamma = 1.8$, while the intrinsic column density and power-law normalization are free. Its absorption-corrected X-ray luminosity is consistent with the standard type 1 AGN relations shown in Figure 2.

J0928 shows a prominent soft residual when fitted with the baseline model and $\Gamma = 1.8$. Allowing Γ to vary improves the fit by $\Delta C = 9.45$ but yields an unusually flat continuum, $\Gamma \sim 0.5$, with negligible intrinsic absorption. Replacing the fully covering absorber with `zpcfabs` improves the fit by a further $\Delta C = 4.73$ and gives $N_{\rm H} = 9.01^{+3.20}_{-3.27} \times 10^{22}$ cm^{-2}, $C_f = 0.94^{+0.04}_{-0.13}$, and $\Gamma = 2.13^{+0.67}_{-0.71}$. J0928 also shows moderately enhanced intrinsic X-ray emission relative to the standard AGN relations.

The simplest interpretation of the two X-normal LLRDs is that they are relatively normal type 1 AGNs hosted by metal-poor dwarf galaxies (from the BPT analysis of R. Lin et al. 2025). A more speculative possibility is that they represent a later evolutionary stage in which an initially LRD-like nucleus is becoming exposed (e.g., S. Fu et al. 2026; R. E. Hviding et al. 2026). This interpretation is motivated by the partial-covering absorber and enhanced X-ray emission of J0928, together with the bluer optical continuum and detected variability of the X-normal LLRDs (R. Lin et al. 2026). In this picture, radiative feedback may have begun to clear the surrounding material, revealing both the central X-ray source and the blue accretion-disk continuum. Further multiwavelength observations are needed to test this evolutionary interpretation.

F. KAPLAN-MEIER ESTIMATE OF THE X-RAY LUMINOSITY DISTRIBUTION

Treating the three undetected sources as left-censored at their tabulated 3σ $\log L^{\rm int}_{2-10}$ limits, we computed a reverse Kaplan–Meier estimate (E. L. Kaplan & P. Meier 1958) for the six individual LLRDs. Its cumulative probability reaches 2/3, 5/6, and 1 at $\log L^{\rm int}_{2-10} = 42.80$, 43.48, and 44.09, respectively; the lowest third remains unresolved

below the detections. With only three detections, and with limits and intrinsic luminosities dependent on the adopted spectral model, we use this estimate descriptively rather than to define the X-normal/X-weak groups.

REFERENCES

Akins, H. B., Casey, C. M., Lambrides, E., et al. 2025, The Astrophysical Journal, 991, 37, doi: 10.3847/1538-4357/ade984

AllWISE Team. 2019, AllWISE Source Catalog, IPAC

An, T., Lin, R., & Wang, A. 2026, arXiv e-prints, arXiv:2610.17559, doi: 10.48550/arXiv.2610.17559

Ananna, T. T., Bogdán, Á., Kovács, O. E., Natarajan, P., & Hickox, R. C. 2024, The Astrophysical Journal Letters, 969, L18, doi: 10.3847/2041-8213/ad5669

Arnaud, K. A. 1996, Astronomical Data Analysis Software and Systems V, 101, 17

Bao, L., Tsai, C.-W., Wu, J., & Wang, J. 2026, arXiv e-prints, doi: 10.48550/arXiv.2605.04685

Bell, E. F., & de Jong, R. S. 2001, The Astrophysical Journal, 550, 212, doi: 10.1086/319728

Bianchi, L. 2020, GALEX UV Unique Source Catalogs (GUVcat) and Cross-Matches With Gaia and SDSS (GUVmatch), STScI/MAST, doi: 10.17909/T9-PYXY-KG53

Bianchi, L., & Shiao, B. 2020, The Astrophysical Journal Supplement Series, 250, doi: 10.3847/1538-4365/aba2d7

Bianchi, L., Shiao, B., & Thilker, D. 2017, The Astrophysical Journal Supplement Series, 230, 24, doi: 10.3847/1538-4365/aa7053

Bock, J. J., Aboobaker, A. M., Adamo, J., et al. 2026, The Astrophysical Journal, 999, 139, doi: 10.3847/1538-4357/ae2be2

Boorman, P. G., Svoboda, J., Stern, D., et al. 2025, The Astrophysical Journal, 988, 157, doi: 10.3847/1538-4357/add727

Brazzini, M., D'Eugenio, F., Maiolino, R., et al. 2026, arXiv e-prints, doi: 10.48550/arXiv.2601.22214

Buchner, J., & Boorman, P. 2023, in Handbook of X-ray and Gamma-ray Astrophysics, ed. C. Bambi & A. Santangelo (Springer Nature Singapore), 1–49, doi: 10.1007/978-981-16-4544-0_175-1

Buchner, J., Brightman, M., Nandra, K., Nikutta, R., & Bauer, F. E. 2019, Astronomy and Astrophysics, 629, A16, doi: 10.1051/0004-6361/201834771

Cappellari, M. 2017, Monthly Notices of the Royal Astronomical Society, 466, 798, doi: 10.1093/mnras/stw3020

Casey, Q. O., Hickox, R. C., Cleri, N. J., et al. 2026, arXiv e-prints, doi: 10.48550/arXiv.2606.26098

Chang, S.-J., Gronke, M., Matthee, J., & Mason, C. 2026, Monthly Notices of the Royal Astronomical Society, 545, staf2131, doi: 10.1093/mnras/staf2131

Chen, C.-H., Shangguan, J., Ho, L. C., et al. 2026, arXiv e-prints, doi: 10.48550/arXiv.2606.04711

Chen, K., Li, Z., Inayoshi, K., & Ho, L. C. 2025, The Astrophysical Journal Letters, 994, L42, doi: 10.3847/2041-8213/ae1955

Chen, S.-J., Buchner, J., Liu, T., et al. 2025, Astronomy and Astrophysics, 701, A144, doi: 10.1051/0004-6361/202554737

Chira, M., Georgakakis, A., Ruiz, A., et al. 2026, Monthly Notices of the Royal Astronomical Society, 545, staf1905, doi: 10.1093/mnras/staf1905

Comastri, A., Lanzuisi, G., Vito, F., et al. 2026, Astronomy and Astrophysics, 706, A302, doi: 10.1051/0004-6361/202557017

Cui, X.-Q., Zhao, Y.-H., Chu, Y.-Q., et al. 2012, Research in Astronomy and Astrophysics, 12, 1197, doi: 10.1088/1674-4527/12/9/003

de Graaff, A., Hviding, R. E., Naidu, R. P., et al. 2025, arXiv e-prints, doi: 10.48550/arXiv.2511.21820

De Luca, V., Franciolini, G., Pani, P., & Riotto, A. 2020, Journal of Cosmology and Astroparticle Physics, 2020, 052, doi: 10.1088/1475-7516/2020/04/052

Ding, W., Kong, X., Guo, W.-J., et al. 2026, Astronomy and Astrophysics, 709, L11, doi: 10.1051/0004-6361/202557889

Done, C., Davis, S. W., Jin, C., Blaes, O., & Ward, M. 2012, Monthly Notices of the Royal Astronomical Society, 420, 1848, doi: 10.1111/j.1365-2966.2011.19779.x

Dong, R., Greene, J. E., & Ho, L. C. 2012, The Astrophysical Journal, 761, 73, doi: 10.1088/0004-637x/761/1/73

EP Science Center. 2024, The Einstein Probe Mission Technical Handbook, EP Science Center. https://ep.bao.ac.cn/ep/cms/files/Cycle3/EP%20Technical%20Handbook.pdf

Fitzpatrick, E. L. 1999, Publications of the Astronomical Society of the Pacific, 111, 63, doi: 10.1086/316293

Fu, S., Zhang, Z., Jiang, D., et al. 2026, Nature Astronomy, doi: 10.1038/s41550-026-02885-8

Greene, J. E., Labbe, I., Goulding, A. D., et al. 2024, The Astrophysical Journal, 964, 39, doi: 10.3847/1538-4357/ad1e5f

Gupta, K. K., Ricci, C., Tortosa, A., et al. 2021, Monthly Notices of the Royal Astronomical Society, 504, 428, doi: 10.1093/mnras/stab839

Hagen, S., Done, C., Silverman, J. D., et al. 2024, Monthly Notices of the Royal Astronomical Society, 534, 2803, doi: 10.1093/mnras/stae2272

Harikane, Y., Zhang, Y., Nakajima, K., et al. 2023, The Astrophysical Journal, 959, 39, doi: 10.3847/1538-4357/ad029e

Hviding, R. E., de Graaff, A., Miller, T. B., et al. 2025, Astronomy and Astrophysics, 702, A57, doi: 10.1051/0004-6361/202555816

Hviding, R. E., de Graaff, A., Liu, H., et al. 2026, The Astrophysical Journal Letters, 1000, L18, doi: 10.3847/2041-8213/ae4c88

Igo, Z., Merloni, A., Georgakakis, A., et al. 2026, arXiv e-prints, doi: 10.48550/arXiv.2607.07795

Inayoshi, K., & Ho, L. C. 2025, arXiv e-prints, doi: 10.48550/arXiv.2512.03130

Inayoshi, K., Kimura, S. S., & Noda, H. 2025, Publications of the Astronomical Society of Japan, 77, psaf050, doi: 10.1093/pasj/psaf050

Izotov, Y. I., Orlitová, I., Schaerer, D., et al. 2016, Nature, 529, 178, doi: 10.1038/nature16456

Ji, X., Maiolino, R., Übler, H., et al. 2025, Monthly Notices of the Royal Astronomical Society, 544, 3900, doi: 10.1093/mnras/staf1867

Ji, X., D'Eugenio, F., Juodžbalis, I., et al. 2026, Monthly Notices of the Royal Astronomical Society, 545, staf2235, doi: 10.1093/mnras/staf2235

Ji, Z., Sun, Y., Giavalisco, M., et al. 2026, arXiv e-prints, doi: 10.48550/arXiv.2606.18342

Jin, C., Done, C., Ward, M., & Gardner, E. 2017, Monthly Notices of the Royal Astronomical Society, 471, 706, doi: 10.1093/mnras/stx1634

Jin, C., Ward, M., & Done, C. 2012, Monthly Notices of the Royal Astronomical Society, 422, 3268, doi: 10.1111/j.1365-2966.2012.20847.x

Juodžbalis, I., Ji, X., Maiolino, R., et al. 2024, Monthly Notices of the Royal Astronomical Society, 535, 853, doi: 10.1093/mnras/stae2367

Juodžbalis, I., Ji, X., D'Eugenio, F., et al. 2026, arXiv e-prints, doi: 10.48550/arXiv.2607.19057

Kaplan, E. L., & Meier, P. 1958, Journal of the American Statistical Association, 53, doi: 10.1080/01621459.1958.10501452

Kennicutt, R. C., & Evans, N. J. 2012, Annual Review of Astronomy and Astrophysics, 50, 531, doi: 10.1146/annurev-astro-081811-125610

Kido, D., Ioka, K., Hotokezaka, K., Inayoshi, K., & Irwin, C. M. 2025, Monthly Notices of the Royal Astronomical Society, 544, 3407, doi: 10.1093/mnras/staf1898

Kocevski, D. D., Finkelstein, S. L., Barro, G., et al. 2025, The Astrophysical Journal, 986, 126, doi: 10.3847/1538-4357/adbc7d

Kubota, A., & Done, C. 2018, Monthly Notices of the Royal Astronomical Society, 480, 1247, doi: 10.1093/mnras/sty1890

Labbe, I., Greene, J. E., Bezanson, R., et al. 2025, The Astrophysical Journal, 978, 92, doi: 10.3847/1538-4357/ad3551

Lambrides, E., Garofali, K., Larson, R. L., et al. 2026, Nature Astronomy, 10, 868, doi: 10.1038/s41550-026-02813-w

Lehmer, B. D., Alexander, D. M., Bauer, F. E., et al. 2010, The Astrophysical Journal, 724, 559, doi: 10.1088/0004-637x/724/1/559

Lin, R., Zheng, Z.-Y., Yuan, F.-T., et al. 2024, Science China Physics, Mechanics, and Astronomy, 67, 109811, doi: 10.1007/s11433-024-2412-3

Lin, R., Zheng, Z.-Y., Jiang, C., et al. 2025, The Astrophysical Journal, 980, L34, doi: 10.3847/2041-8213/adaaf1

Lin, R., Zheng, Z.-Y., Wang, J., et al. 2026, The Astrophysical Journal, 1005, 150, doi: 10.3847/1538-4357/ae74c6

Lin, X., Fan, X., Cai, Z., et al. 2026a, The Astrophysical Journal, 997, 364, doi: 10.3847/1538-4357/ae2bdf

Lin, X., Fan, X., Cai, Z., et al. 2026b, arXiv e-prints, doi: 10.48550/arXiv.2605.21574

Liu, H., Jiang, Y.-F., Quataert, E., Greene, J. E., & Ma, Y. 2025, The Astrophysical Journal, 994, 113, doi: 10.3847/1538-4357/ae0c19

Liu, J., Feng, H., & Ho, L. C. 2026, arXiv e-prints, doi: 10.48550/arXiv.2607.17448

Liu, S., Luo, A.-L., Zheng, Z., et al. 2024, Astronomy and Astrophysics, 689, A170, doi: 10.1051/0004-6361/202449406

Liu, T., Buchner, J., Nandra, K., et al. 2022, Astronomy and Astrophysics, 661, A5, doi: 10.1051/0004-6361/202141643

Madau, P., & Maiolino, R. 2026, arXiv e-prints, doi: 10.48550/arXiv.2602.22386

Maiolino, R., Risaliti, G., Signorini, M., et al. 2025, Monthly Notices of the Royal Astronomical Society, 538, 1921, doi: 10.1093/mnras/staf359

Matthee, J., Naidu, R. P., Brammer, G., et al. 2024, The Astrophysical Journal, 963, 129, doi: 10.3847/1538-4357/ad2345

Matthee, J., Torralba, A., Pezzulli, G., et al. 2026, arXiv e-prints, doi: 10.48550/arXiv.2603.17667
Mezcua, M. 2017, International Journal of Modern Physics D, 26, 1730021, doi: 10.1142/s021827181730021x
Mineo, S., Gilfanov, M., & Sunyaev, R. 2012, Monthly Notices of the Royal Astronomical Society, 426, 1870, doi: 10.1111/j.1365-2966.2012.21831.x
Morrissey, P., Conrow, T., Barlow, T. A., et al. 2007, The Astrophysical Journal Supplement Series, 173, 682, doi: 10.1086/520512
Naidu, R. P., Matthee, J., Katz, H., et al. 2025, arXiv e-prints, doi: 10.48550/arXiv.2503.16596
Nedkova, K. V., Häußler, B., Marchesini, D., et al. 2021, Monthly Notices of the Royal Astronomical Society, 506, 928, doi: 10.1093/mnras/stab1744
Ni, Q., Brandt, W. N., Luo, B., et al. 2018, Monthly Notices of the Royal Astronomical Society, 480, 5184, doi: 10.1093/mnras/sty1989
Pacucci, F., & Narayan, R. 2024, The Astrophysical Journal, 976, 96, doi: 10.3847/1538-4357/ad84f7
Pan, Z., Zhuang, M.-Y., Shen, Y., et al. 2026, arXiv e-prints, arXiv:2606.09721, doi: 10.48550/arXiv.2606.09721
Planck Collaboration, Aghanim, N., Akrami, Y., et al. 2020, Astronomy & Astrophysics, 641, A6, doi: 10.1051/0004-6361/201833910
Rinaldi, P., Rieke, G. H., Wu, Z., et al. 2026, The Astrophysical Journal, 1006, 205, doi: 10.3847/1538-4357/ae80cd
Rusakov, V., Watson, D., Nikopoulos, G. P., et al. 2026, Nature, 649, 574, doi: 10.1038/s41586-025-09900-4
Sacchi, A., & Bogdán, Á. 2025, The Astrophysical Journal, 989, L30, doi: 10.3847/2041-8213/adf5c8
Seppi, R., Comparat, J., Bulbul, E., et al. 2022, Astronomy and Astrophysics, 665, A78, doi: 10.1051/0004-6361/202243824
Setton, D. J., Greene, J. E., Spilker, J. S., et al. 2025, The Astrophysical Journal Letters, 991, L10, doi: 10.3847/2041-8213/ade78b
Simmonds, C., Bauer, F. E., Thuan, T. X., et al. 2016, Astronomy and Astrophysics, 596, A64, doi: 10.1051/0004-6361/201629310
Sneppen, A., Watson, D., Matthews, J. H., et al. 2026, arXiv e-prints, doi: 10.48550/arXiv.2601.18864
Spherex Team. 2025, SPHEREx Quick Release Spectral Images - QR2, IPAC, doi: 10.26131/IRSA652
Tange, O. 2011, USENIX Magazine, 36, 42
Taylor, M. B. 2005, in Astronomical Society of the Pacific Conference Series, Vol. 347, Astronomical Data Analysis Software and Systems XIV, ed. P. Shopbell, M. Britton, & R. Ebert, 29
Wang, B., Leja, J., Katz, H., et al. 2026, The Astrophysical Journal, 1003, 10, doi: 10.3847/1538-4357/ae5bab
Weibel, A., Oesch, P. A., Barrufet, L., et al. 2024, Monthly Notices of the Royal Astronomical Society, 533, 1808, doi: 10.1093/mnras/stae1891
Wright, E. L., Eisenhardt, P. R. M., Mainzer, A. K., et al. 2010, The Astronomical Journal, 140, 1868, doi: 10.1088/0004-6256/140/6/1868
Yan, Z., Inayoshi, K., Chen, K., & Guo, J. 2026, The Astrophysical Journal, 1002, 159, doi: 10.3847/1538-4357/ae5dbd
Yang, H., Malhotra, S., Gronke, M., et al. 2016, The Astrophysical Journal, 820, 130, doi: 10.3847/0004-637x/820/2/130
Yuan, G.-W., Lei, L., Wang, Y.-Z., et al. 2024, Science China Physics, Mechanics, and Astronomy, 67, 109512, doi: 10.1007/s11433-024-2433-3
Yuan, W., Dai, L., Feng, H., et al. 2025, Science China Physics, Mechanics, and Astronomy, 68, 239501, doi: 10.1007/s11433-024-2600-3
Yue, M., Eilers, A.-C., Ananna, T. T., et al. 2024, The Astrophysical Journal Letters, 974, L26, doi: 10.3847/2041-8213/ad7eba
Zhang, C., Wu, Q., Fan, X., et al. 2026, Nature Astronomy, 10, 753, doi: 10.1038/s41550-026-02785-x
Zhang, Z., Jiang, L., Liu, W., & Ho, L. C. 2025, The Astrophysical Journal, 985, 119, doi: 10.3847/1538-4357/adcb3e
Zhou, S., Sun, M., Ji, X., et al. 2026, arXiv e-prints, doi: 10.48550/arXiv.2606.21105
Zhuang, M.-Y., Li, J., Shen, Y., et al. 2026, The Astrophysical Journal, 999, 31, doi: 10.3847/1538-4357/ae3612